High-fidelity Aerodynamic and Acoustic Evaluations of a Heavy-lift eVTOL in Hover

Tao Zhang [1]
School of Engineering, University of Leicester, Leicester, U.K.
George N. Barakos [2]
CFD Laboratory, School of Engineering, University of Glasgow, Glasgow, U.K.
Furqan [3] , Malcolm Foster [4]
GKN Aerospace, Bristol, U.K.

Abstract

This paper presents a high-fidelity aerodynamic and acoustic evaluation in hover of a heavy-lift eVTOL design. The design, known as Skybus, has an MTOW of 14,000kg, and six tiltable rotors attached at the tip of three sets of tandem wings with flaps. High-fidelity CFD simulations of the entire Skybus vehicle in hover were conducted using the HMB3 framework with scale-adaptive turbulence modelling. The simulations considered three design variations with revised airframe and blades and resolved complex flow details. The aerodynamic performance, blockage, and interactions were analysed in detail. The baseline airframe caused a blockage force of about 13% of the MTOW. The hovering rotors in compact configurations induced a sinusoidal single-blade loading variation, blended with small local interactions corresponding to blade encounter and rotor-wing interactions. However, the overall loading variations were small and were within 1% of the MTOW. Further, the near-field acoustics was directly extracted from the high-fidelity CFD results, and far-field acoustic propagation was computed using the acoustic analogy. The design modifications caused strong impact on the vehicle acoustics because of different aerodynamic interactions, and of the propeller acoustic characteristics. In the far field and below the hovering vehicle, the acoustic directivity was along the longitudinal direction, especially ahead of the cockpit. Tonal corrections were also performed to compute the effective perceived noise level (EPNL) in certification scenarios. The Skybus design showed about 95 EPNdB assuming a 2-min hover duration, which was below the certification limit of equivalent helicopters.

1 Introduction

Recently, the Advanced Air Mobility (AAM) concept has drawn remarkable attention from industry and academia. It represents a significant breakthrough in urban transportation, promising improved efficiency, sustainability, and connectivity. Nonetheless, the development of AAM vehicles faces several technical challenges [1] due to significant knowledge gaps. To date, a booming number of AAM conceptual designs have been unveiled by start-ups or large aerospace companies. Yet, few have demonstrated some flight capabilities and are still far from service or certification.

Aerodynamics remains a major challenge for AAM development. Current AAM designs adopt radical configurations to meet unconventional needs for safety, efficiency, and versatility. These novel configurations usually combine multiple rotary wing systems and lifting surfaces, and are often convertible for different flight regimes. This leads to intense and complex aerodynamic interactions between rotors, lifting surfaces, and the airframe, and may, consequently, cause strong performance variations and acoustic radiation. The lack of accurate data and understanding of these aerodynamic interactions hinders the AAM development., and the evolution of designs. The adoption of electrical motors for greener aviation adds extra complexity to the aerodynamics, with RPM rotor regulations. As test data of AAM designs are scarce, and expensive at this stage,

[1]Lecturer - tz77@leicester.ac.uk
[2]Professor - george.barakos@glasgow.ac.uk
[3]Technical Authority – Advanced Air Mobility, GKN Aerospace - furqan@gknaerospace.com
[4]Director - Special Projects, GKN Aerospace - Malcolm.Foster@gknaerospace.com

numerical modelling is the most feasible approach to improve our understanding of AAM aerodynamics.

High-fidelity Computational Fluid Dynamics (CFD) is essential for modelling AAM, as low-fidelity approaches (e.g. lifting lines, blade element methods, and panel methods) struggle to handle the inherently vortical, unsteady, and interactional flow physics. In recent years, several research works have reported applying high-fidelity CFD modelling to unconventional AAM designs, including the thrust-augmented RACER design [2, 3, 4, 5, 6], the NASA quad-rotor and side-by-side conceptual design [7, 8, 9], and the distributed lift Volocopter-2X configuration [10, 11, 12]. Studies focusing on interactions between particular components, e.g. rotor-rotor interactions [13, 14, 15] and rotor-wing interactions [16, 17, 18], are also noted. To resolve the complex flow physics and handle the complex geometries and their motions/deformations, state-of-the-art techniques, e.g. high-order schemes, advanced turbulence modelling, overset grids, high-performance computing etc were used. With accurate modelling, these studies reported important and complex aerodynamic interactions among rotors, lifting surfaces, and airframes. Few investigations [9, 19] focused on acoustic performance, and reported substantial impact of the aerodynamic interactions. As experimental campaigns slowly ramp up [20, 13], these detailed numerical investigations continue to provide valuable guidance for AAM development.

Current AAM designs and studies predominantly focus on small-size vehicles for use as personal aerial transport or air taxis. Small-size designs bring advantages such as simple infrastructure requirements, better accessibility, and lower noise emission. On the other hand, large-scale designs are eventually desirable for heavy-lift missions, increased cargo/passenger capacity, and fewer mission entries. However, the large vehicle size and weight pose significant challenges, including the ground infrastructure, operation rules, aerodynamic performance, and noise emissions due to heavy disk loadings. Yet, few relevant studies can be found in the public domain. In light of this, GKN Aerospace proposed the Skybus [21, 22] heavy-lift eVTOL (electrical Vertical Take-off Landing) design as part of a feasibility study under the UK ISCF Future Flight Challenge. Skybus aims to take the ‘Park and Ride’ concept into the air for mass public transport over extremely congested routes. One application looks at commuting between the London M25 and the centre of London at a maximum capacity of 30 passengers within 15 minutes.

At this preliminary stage, the Skybus vehicle is designed as a multi-rotor compound rotorcraft, with three sets of tandem wings and six wing-tip-mounted, tiltable propellers. The designed MTOW (Maximum Take-off Weight) is 14,000kg. In hover, and during take-off/landing, the propellers tilt vertically to provide lift. In cruise flight, all propellers tilt horizontally to provide propulsion or are feathered for minimised drag. The tandem wings provide the cruise lift. Skybus is fully electric-powered for reduced emissions. The electric motors provide the propellers with both pitch and RPM regulations to accommodate different thrust requirements for different flight regimes.

Our previous studies [21, 22] have systematically analysed the propeller design and aerodynamic/acoustic performance in cruise. This study complements our previous work and focuses on hover aerodynamic/acoustic performance. For the Skybus vehicle, the hover flow physics is particularly complex, due to the high disk loading and wake interactions with wings and airframe. The noise emission in hover is of primary concern, since the hover flight regime mostly corresponds to take-off/landing, where we have the minimal source-receiver distance and maximised noise impact on humans.

The Skybus is still in the preliminary design stages thus significant acoustic design/optimisation opportunities remain and have yet to be explored. The objectives of this study are hence to evaluate the aerodynamic and acoustic performance of the heavy-lift Skybus design in hover flight, and to assess performance variations subject to design improvements through high-fidelity CFD modelling. In this work, high-fidelity CFD simulations of the complete Skybus vehicle in hover were carried out using the Helicopter Multi-Block 3 (HMB3) framework [23], with fully-structured Chimera grids and Scale-Adaptive Simulations (SAS) [24] of turbulence. The complex geometries were meshed and resolved in detail, including the wing flaps and nacelles, and a grid convergence study was also conducted. Three configurations with revised airframe and propeller designs were modelled, and the aerodynamic performance was compared in detail. The loadings and interactions on the airframe and the rotors were extracted and discussed. Further, the near-field acoustic features of the heavy-lift eVTOL were extracted from the high-fidelity CFD results, and the far-field acoustic propagation was computed through acoustic analogy. The acoustic strength, spectral components, and human perception in noise certification scenarios were analysed in detail.

2 Numerical Methods

2.1 Helicopter Multi-Block 3 (HMB3) Framework

The Helicopter Multi-Block 3 (HMB3) [23, 25] framework is a high-fidelity CFD framework consisting of high-order CFD solvers with advanced turbulence modelling capabilities, overset/sliding/deforming mesh capabilities, adjoint solvers and harmonic balance methods, acoustic solvers, and elastic modules, along with a complete toolchain. It has well-established capabilities for high-fidelity aerodynamic, aero-acoustic, and aero-elastic analysis and multi-disciplinary optimisation. It has also been widely used in simulations of rotorcraft flows [26, 27, 28, 29, 14].

As the framework's core, the HMB3 flow solver solves the Unsteady Reynolds Averaged Navier-Stokes

(URANS) equations in integral form using the Arbitrary Lagrangian Eulerian (ALE) formulation for time-dependent domains, which may include moving boundaries. The Navier-Stokes equations are discretised using a cell-centred finite volume approach on multi-block, structured grids:

$$\frac{d}{dt}\left(\mathbf{W}_{i,j,k}V_{i,j,k}\right) = -\mathbf{R}_{i,j,k}\left(\mathbf{W}_{i,j,k}\right), \qquad (1)$$

where i,j,k represent the cell index, $\mathbf{W}$ and $\mathbf{R}$ are the vector of conservative flow variables and residual respectively, and $V_{i,j,k}$ is the volume of the cell i,j,k. To evaluate the convective fluxes, Osher's approximate Riemman solver is used, while the viscous terms are discretised using second-order central differences. The 3^{rd} order MUSCL (Monotone Upstream-centered Schemes for Conservation Laws) approach was adopted to provide high-order accuracy in space. The chimera/overset grid method [30] was extensively used in this work.

To resolve the complex flow physics of the Skybus vehicle in hover flight, the Scale Adaptive Simulation (SAS) was adopted for the turbulence modelling. SAS is capable of resolving the turbulent spectrum in unsteady flow regions, while also operating in standard RANS mode. The SAS concept was proposed by Menter and Egorov [31, 32], based on Rotta's model [33] considering the integral length scale. For the k-ω SST model, the SAS capability can be added by an extra source term to the dissipation rate. It automatically balances the contributions of modelled and resolved turbulent stress, much like the hybrid LES/RANS approach, but it has a weaker dependence on the grid cell size and has a moderate computational cost. More details of the formulations, constants, and implementations in HMB3 can be found in Refs[31, 24].

2.2 Acoustic Computations

In the present study, the near-field acoustics was directly computed from pressure fields resolved by high-fidelity HMB3 simulations. The sound pressure signals were extracted by subtracting the time-averaged means. This direct approach included all acoustic sources in the near-field, subject to the CFD resolution. This approach has been used in acoustic analyses of propellers, ducted propellers, and eVTOL vehicles using HMB3 [34, 35, 36, 22].

This direct approach requires high-order schemes and fine spatial/temporal resolution. For the current acoustic study, the 3rd-order MUSCL scheme was used. The near-field background grid was carefully tuned to guarantee at least 10 mesh points for the wavelength at 20 times the Blade Passing Frequency (BPF = 33.8 Hz) in the 16-metre proximity. Most near-field acoustic evaluations were carried out within 15- to 20-metre proximity of the vehicle. The simulations adopted a temporal resolution of 0.5 degrees of the azimuth per time step, corresponding to at least 120 sampling points for the dominant BPF.

The far-field acoustics was efficiently calculated using the FW-H equation [37], following the Farassat Formulation 1A [38], taking as input CFD solutions of the surface pressure fields. The formulation has been widely used for far-field noise predictions of aircraft, wind turbines [39], and propellers [35, 40, 41, 22].

The current far-field acoustic computations were carried out using the in-house acoustic solver HFWH2 (Helicopter Ffows Williams-Hawkings 2) [35, 41]. Extensive code-to-code comparisons have also been performed to verify the current implementation [40]. The current far-field acoustic approach focused on the non-porous formulation and ignored the quadrupole source, which requires expensive integrations over volumes. This was due to the subsonic nature of the current simulation, and the propeller tip Mach number was about 0.34.

3 Test Matrix, Numerical Settings, and Grid Convergence Study

The hover investigation of the Skybus design focused on 3 configurations as shown in Figures 1(a) to 1(c). Configuration C1 in Figure 1(a) was the baseline configuration to start the investigations. C1 had 3 sets of tandem wings mounted on top of the fuselage. The front wing had a 5-deg anhedral angle, and the aft wing had a 10-deg dihedral for forward flight efficiency [22]. All wings were equipped with flaps to reduce the rotor downwash in hover. The front and aft wings have full span flaps, while the middle wing flap was only installed in areas under the rotor. All these flaps were meshed and fully resolved in the simulations. Six propellers were attached at the wing tips with their nacelles. The propellers and nacelles were tilted vertically to provide hover capability. All blades and nacelles were meshed and resolved in the numerical modelling. All propellers had 6 blades with the same blade design reported found in earlier studies [21, 22]. In hover, these rigid propellers had pitch and RPM regulations without flapping mechanisms. In forward flight, they are tilted horizontally and operate at different pitch/RPM settings to counter the overall vehicle drag, with the wings providing the required lift. Aerodynamic and acoustic performance of the Skybus in forward flight can be found in Ref [22]. Note that due to the an-/dihedral angles of the front and aft wings, the propeller disks were not aligned at the same vertical plane. From front to aft, the disk positions were gradually increased. This design reduces the rotor interactions in transition and forward flight. Note that there was no overlap between the rotors.

Configuration C2 in Figure 1(b) was derived by revising the fuselage and wing shapes of C1. The modifications aimed to reduce the aerodynamic interactions between components. As shown in Figure 1(b), the fuselage of C2 was narrower and longer than C1. The wing shapes, including sectional shapes, flap locations,

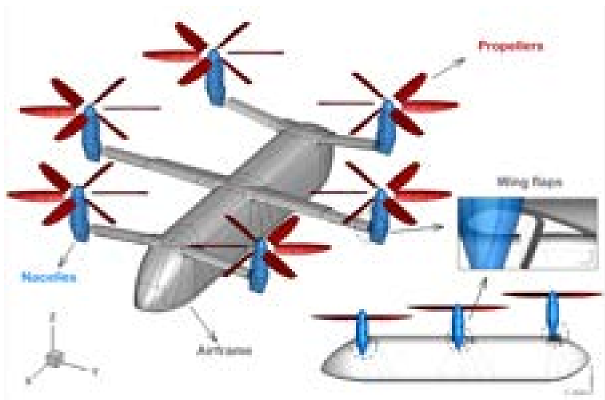

(a) Configuration C1 (baseline).

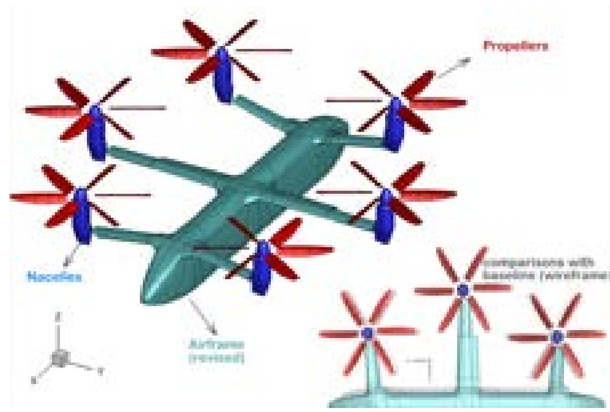

(b) Configuration C2 (revised airframe).

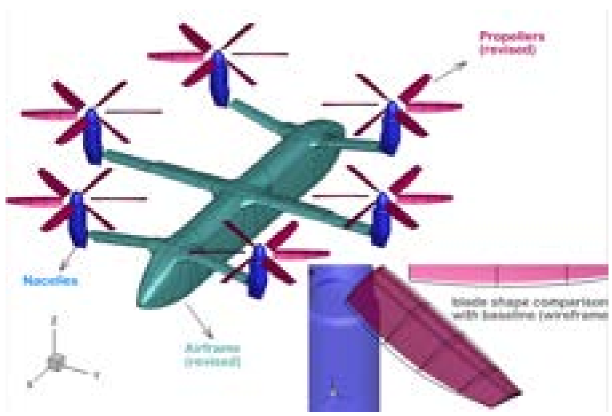

(c) Configuration C3 (revised airframe and revised blades).

Figure 1: Geometries of the studied aircraft configurations.

Table 1: Hover flight conditions.

Flight Conditions	
-MTOW	14,000 kg
-Altitude	sea level (OGE)
-Airframe attitude	level (zero yaw/pitch/roll)
-Trimming target	L = MTOW

installation angles, and an-/dihedral angles, remained unchanged. The wing roots were slightly extended to connect to the shrunk fuselage. The front wing was also added a 5-deg forward swept, while the aft wing received a 5-deg backward swept. This separated the front and aft propellers from the middle ones by 25 cm in the longitudinal direction.

Configuration C3 in Figure 1(c) was derived from C2 with revised blade shape designs. The propellers were optimised using adjoint-based optimisation [21] ignoring installation effects. The multi-point optimisation reduced the propeller torque by 5% in hover, and 3% in forward flight while maintaining the respective thrust. Compared to the original design, the optimised blade had increased blade twist, decreased chord, and increased sectional camber.

Table 1 presents the flight conditions in hover, while Table 2 presents the propeller operating conditions. The hover simulation was carried out at sea level out of ground effects (OGE). The Maximum Take-off Weight (MTOW) was about 14,000 kg. As detailed in Table 2, in simulations, all propellers had the same pitch ($\beta_{0.75}$ = 23.8 deg) and RPM = 338 sharing the same phase. The corresponding blade tip speed was about Ma = 0.34. Note that propellers on the starboard and port sides were symmetric in geometry and motion. All starboard-side propellers rotated clockwise as viewed from above, while all port-side propellers rotated counter-clockwise viewed from above. This arrangement enabled symmetry planes to be used in the numerical modelling to reduce the computational domain by half. The symmetry also eliminated the need for yawing and rolling trimming. In hover simulations, the trimming target was to meet the MTOW of 14,000 kg. The pitching moment was not considered in the trimming since the vehicle's centre of gravity was yet to be decided. The propeller settings of RPM = 338 and $\beta_{0.75}$ = 23.8 deg were interpolated from the isolated propeller performance maps, with an overestimate of 15% to account for downwash.

Figure 2 presents the overset grid topology for the hover simulation using HMB3. All configurations C1, C2, and C3 used the same grid system, with modified multi-block mapping. Symmetry planes were used to reduce the computational cost. Four levels of fully-structured grids were generated separately for each component, assisted by automatic meshing tools [42], and were then assembled using overset approaches [30] for the numerical modelling with the third-order MUSCL scheme [43]. The Reynolds number based on the rotor radius (reference length) and tip speed was about $Re = 2.6 \times 10^7$. The SAS model [24] was adopted for the turbulence modelling. All boundary layer grids were carefully tuned to ensure $y^+ \leq 1$. The near-body grid resolution near the blades was about $0.1C$ where C is the blade chord at 75% span. This $0.1C$ resolution was kept in the fine background grid within about 5 blade radii around the vehicle, corresponding to about 10 points per wavelength, at 20 times the blade passing frequency (BPF). From 5 to 10 radii, the resolution was gradually reduced to about $0.5C$, then to about $20C$ in the far-field, 25 radii away.

A grid convergence study was carried out on configuration C1 using 3 sets of grids with varying densities as detailed in Table 3. It is difficult to systematically vary the cell numbers for overset grids, because lower-level grids must provide enough interpolation cells for higher-level components. The coarse, medium, and fine grids used in this work were composed by carefully varying the near- and off-body components. For the half-model simulation with symmetry planes, the coarse, medium, and fine grids had 65.48, 87.26, and 116.4 million cells in total, respectively. The fine grid used about 1/3 of the total cell counts in the background for the wake resolution. The overall grids had a consistent refinement ratio of 1.33 from coarse to medium and from medium to fine. For this grid convergence study, simulations were carried out at a time step size of $1 - deg\ /step$ for the rotors, corresponding to 1/60 of dominant flow periodicity (one blade passage). For later aerodynamic/acoustic investigations, the time step size was reduced to $0.5 - deg\ /step$ for the acoustic resolution, but integrated aerodynamic loads showed negligible changes.

Figures 3(a) to 3(c) present the flow solutions using the coarse, medium, and fine grids of Table 3. The flow features are presented as iso-surfaces of dimensionless Q-criterion coloured by vorticity magnitudes. The solutions were copied and mirrored to comprise the full vehicle. The Scale-Adaptive simulations resolved abundant flow details like rotor vortices, downwash, separated flow regions, and complex interactions between components. From the coarse grid in Figure 3(a) to the medium grid in Figure 3(b), the wake resolution was only slightly improved. This was because only near-body regions were refined from Figure 3(a) to Figure 3(b). After further improving the background mesh resolution, the wake was considerably improved as shown in the fine grid solution of Figure 3(c). It was clearly shown that rotor wake impinges upon the airframe, induces complex secondary flow features, and gradually breaks down to complex smaller vortices as being convected away by the downwash. Nonetheless, due to interpolation, the flow features were slightly dissipated while passing through overset boundaries.

Figure 4 presents the Richardson extrapolation [44] of the total lift predictions using the 3 grids of Table 3. As the cell size was reduced, the overall lift prediction showed clear trends of convergence. The difference be-

Table 2: Propeller operating conditions. All propellers have the same blade design but are symmetric about the lateral centre.

Propeller Operation	
-Operating propellers	6
-Tilt angle	90° (vertical)
-Operating condition (RPM, $\beta_{0.75}$)	(338, 23.8°)
-Blade tip Mach	0.34
-Rotation direction (viewed from above)	CW(star-board-side)/ CCW (port-side, symmetry)
-Phase delay	0°(synchronised)

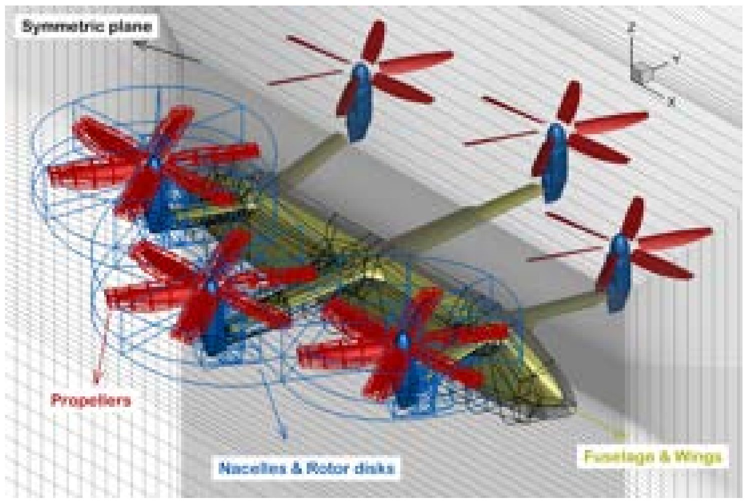

Figure 2: Grid topology for the Skybus hover simulations using Chimera grids.

Table 3: Grid details of the mesh sensitivity study for the hover simulations. The numbers denote millions of cells in the mesh components.

Grids	Off-body	Near-body			Total near-body	Total	Refinement ratio / [-]
		fuselage	nacelles	blades			
Coarse	19.86	12.86	15.3	17.46	45.62	65.48	-
Medium	19.86	12.86	15.3	39.24	67.4	87.26	1.33
Fine	33.1	12.86	31.2	39.24	83.3	116.4	1.33

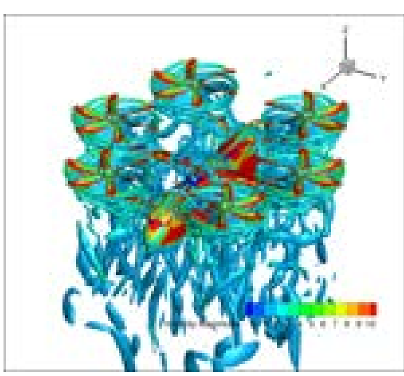

(a) Coarse grid.

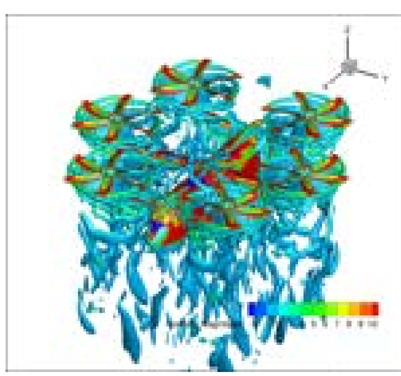

(b) Medium grid.

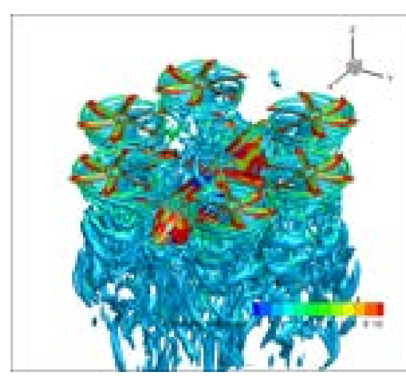

(c) Fine grid.

Figure 3: Flow solution obtained using three grid levels.

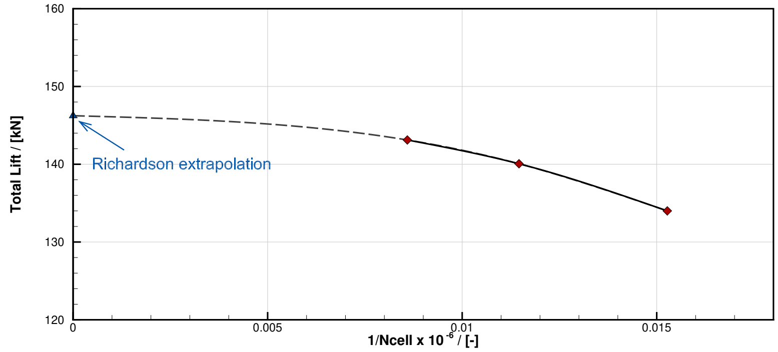

Figure 4: Total lift predictions and Richardson extrapolation.

Table 4: Grid Convergence Index (GCI) and GCI ratio values of the mesh convergence study.

	Refinement Ratio	GCI	GCI Ratio
Coarse-Medium	1.33	2.79×10^{-2}	1.045
Medium-Fine	1.33	5.77×10^{-2}	

tween the fine- and medium-grid predictions was about 4 kN or 2.9% of the MTOW. This small difference was brought by the improved wake resolution. The extrapolated lift at zero cell size was about 2 kN higher than the fine-grid prediction, a tiny difference corresponding to about 1.46% of the MTOW. The spatial accuracy of the modelling was estimated to be of the order of 2.4, using Richardson extrapolation and the grids of Table 3. This was slightly lower than the intended third-order accuracy but was reasonable due to losses through overset regions. Table 4 presents the Grid Convergence Index (GCI) and GCI ratio [44] between the two refinement levels. In the current work, the GCI ratio was 1.045, which is close enough to unity, suggesting that the grids and modelling have reached the asymptotic region of convergence. Later investigations of aerodynamic loadings and far-field acoustics of configurations C2 and C3 hence used the medium grid system to reduce the computational cost.

4 Analysis of Aerodynamic Interactions

4.1 Overall Aerodynamic Loading Analysis

This section presents detailed analyses and comparisons of interactional aerodynamics between the three configurations C1, C2, and C3. From the perspective of vehicle design and operation, the steady/unsteady aerodynamic loads are of primary interest. Figures 5(a) and 5(b) first present the contributions of each component to the overall lift and power consumption. The lift and power values were time averaged over the last rotor revolution.

In Figure 5(a), all lift forces were normalised using the MTOW. For configuration C1, the overall lift is about 1.02 times the MTOW, with each pair of propellers contributing about 0.38 MTOW lift. The airframe and nacelles caused a blockage force of about 0.13 MTOW. After revising the fuselage and airframe shapes in configuration C2, the blockage was reduced to 0.10 MTOW. The propeller lift contributions showed negligible changes. The overall lift was slightly increased to 1.06, mainly due to the reduced airframe blockage. As for configuration C3 with the revised blade design, the averaged propeller thrust varied little. There was 0.01 MTOW reduction in thrust for both middle and aft propellers. The airframe blockage was also reduced by 0.01 MTOW, which should be associated with the reduced propeller thrust. The overall lift was about 1.04 MTOW.

Regarding the time-averaged lift, all configurations generated the required lift close to the trimming target in hover, i.e. the MTOW. All propellers produced a similar thrust of 0.19 despite their different installation positions. The initial airframe of C1 caused a blockage force of 0.13 MTOW, and this was reduced to about 0.10 MTOW by revising the airframe design as shown in Figure 1(b). This suggests that the airframe blockage to a single propeller was not substantial in this hover condition, as the 0.10 MTOW blockage was distributed among 6 propellers.

In Figure 5(b), all power values were time-averaged over one propeller revolution and normalised by the overall power consumption (P_0) of configuration C1. In hover, all power was consumed by the propellers hence the airframe and nacelles were excluded. For configuration C1, the power was almost evenly consumed by each propeller. This was the same for configuration C2, except that the middle propeller power was very slightly increased by 0.01 P_0. The apprent discrepancy between the overall and component power was due to round-off errors. As for configuration C3 with the revised propeller, the overall power was reduced to about 0.97 P_0. This 3%

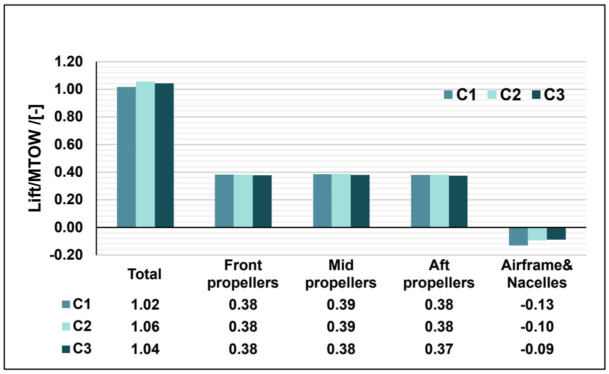

(a) Total and component lift contributions.

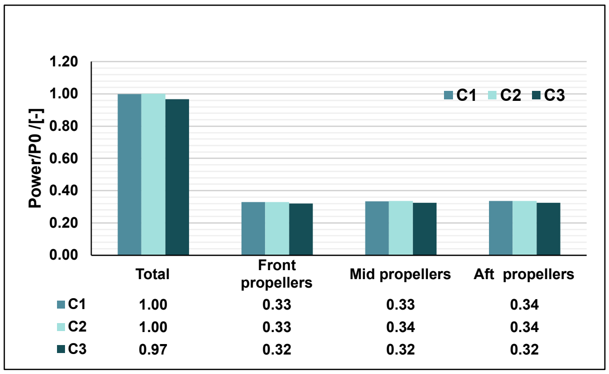

(b) Total and propeller power consumptions.

Figure 5: Time-averaged lift and power breakdown of the 3 configurations in hover.

power reduction was expected, as was suggested by the multi-point shape optimisation, although the benefit was lower than the 5% expectation due to installation effects. The power was still evenly consumed by the propellers, with each pair having a 0.01 to 0.02 P_0 reduction.

Figures 6(a) to 6(b) present analyses of the unsteadiness of the integrated lift. Figure 6(a) shows the lift variations around azimuth over one propeller revolution for the three configurations. The lift forces were normalised by the vehicle MTOW. For all three configurations, the lift curve showed similar periodicity with 6 major peaks per revolution, i.e. the blade passing frequency (BPF). However, there are complex low- and high-frequency components.

Figure 6(b) presents the frequency analysis of the signals using Fast Fourier Transformation (FFT). The frequencies were normalised by the BPF of 33.8 Hz to highlight the correlations. For all configurations, the lift variations primarily corresponded to the BPF and its harmonics. The variations had rich high-frequency components, indicating strong interactions caused by the rotating blades. All configurations had similar similar low-frequency components up to about the 5th BPF. For higher frequencies, all configurations had peaks at harmonics of the BPF, but the magnitudes varied. This suggests that the blade motion is the dominant source of unsteadiness for all three configurations in hover. All three configurations shared the same primary low-frequency variations with the same blade motions. Differences in the geometries mostly led to high-frequency variations.

4.2 Airframe Loading and Interactions

The time-averaged forces due to downwash on the airframe for all configurations are presented in Table 5, along with the standard deviations (σ) indicating the unsteadiness levels. All values were normalised by the MTOW to highlight their impacts in hover. For configurations C1, C2, and C3, the overall loading on the airframe corresponded to 13%, 10%, and 9% of the MTOW as shown in Figure 5(a), respectively. Table 5 suggests that the wing contributions were similar for C1 and C2 despite the differences in the airframe. The front and middle wings showed blockage forces of about 2.4% MTOW. Note that the middle wing had a longer span while its blockage was similar to the front wing, indicating that the front wing blockage was more severe. The aft wing blockage was slightly lower at about 1.6% MTOW. The standard deviations were negligible for all wings, but the front wing showed a slightly higher level of fluctuations. The same held for C3, but the wing loadings were reduced by about 0.1% MTOW due to the reduced rotor loading. In total, the wings contributed about 6% MTOW blockage and the standard deviations were negligible.

The fuselage blockage showed major changes subject to the design changes. Configuration C1 showed a fuselage blockage of about 6.1% MTOW, and this was halved to 3% with the revised airframe design in C2. In C3, with slightly reduced disk loadings, this was further reduced to 2.1%. The standard deviations of the fuselage loading were still small, but they were one order of magnitude higher relative to the wing loadings.

Figures 7(a) to 7(b) present the time-averaged surface pressure coefficient distributions on the airframes for configurations C1, C2, and C3, normalised with the rotor tip speed. The stagnation pressure on the airframe was present on the wing surfaces right beneath the rotors. High-pressure regions were also noted at wing-fuselage junctions, especially for the front and aft wings. Low-pressure regions were mostly noted at the wing leading edges and flap surfaces. However, the maximum and minimum C_P magnitudes were of about ± 0.1 using the blade tip dynamic head, suggesting that the overall integrated pressure forces were small compared to the rotor loading.

4.3 Rotor Loading and Interactions

This section discusses the rotor loadings and the occurring aerodynamic interactions. Table 6 presents the time-averaged single rotor thrust along with the standard deviations indicating the unsteadiness levels. All values were normalised using the MTOW. For all configurations, each rotor carried about 19% of the MTOW, with a negligible amount of deviation, less than 0.5% of the MTOW. The front rotor deviations were very slightly

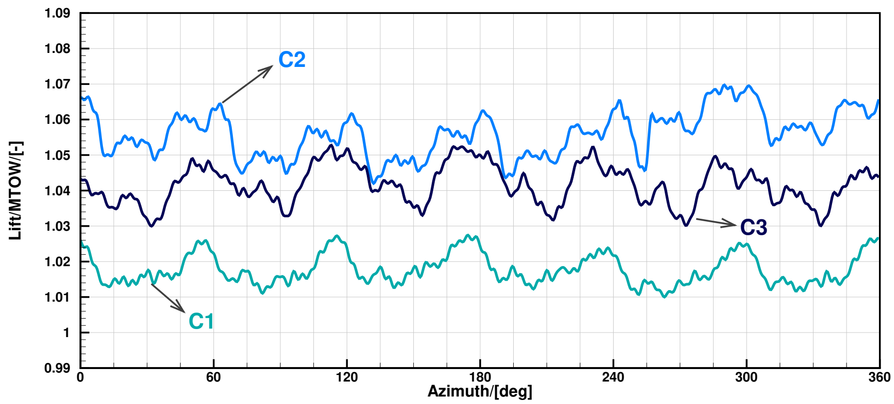

(a) Total lift azimuthal variations.

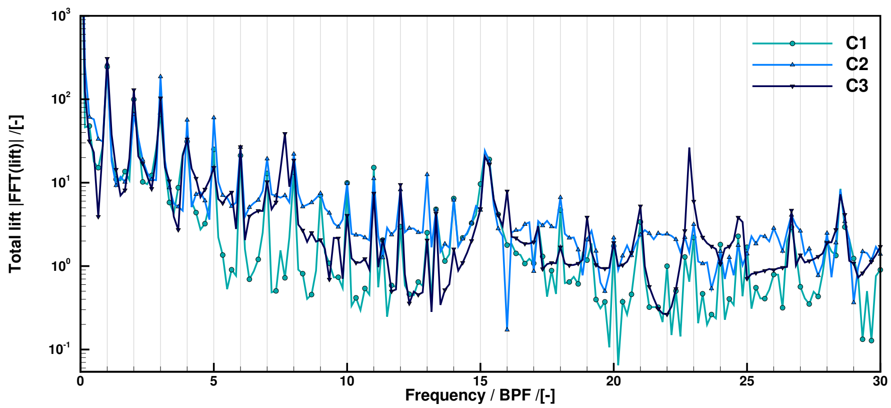

(b) Total lift frequency content.

Figure 6: Temporal variations and frequency content of the overall lift variations.

higher than the middle and aft rotors. The rotors of C3 produced slightly lower thrust due to their revised design.

Single-blade loading variations, with azimuth Ψ, were extracted and presented in Figures 8(a) to 8(c) for all configurations. The single-blade loading had sinusoidal patterns with small fluctuations corresponding to specific interactions. Despite differences in the geometry, all configurations showed very similar loading variations and fluctuations. The following analyses will hence focus on the C1 configuration.

The disk thrust distributions for C1 are shown in Figure 9. Note that these are thrust changes relative to the isolated case to highlight installation effects and interactions. Despite the hover condition, all propellers showed unbalanced and complex disk loadings. In general, all propeller disks had increased tip loading in outwards regions and reduced loading in regions facing the airframe. This was also observed in previous investigations of rotors in compact configurations [12]. The rotors induced a stronger downwash convecting the wake systems in the central area. This caused thrust decreases in the inner regions. The tip thrust of the outer regions was increased due to stronger wake contractions towards the airframe.

Nevertheless, the interactions between rotors and airframe added more complexity to the loading distribution. As already mentioned, the three propellers were staggered vertically due to the wing an-/dihedral angles. Because of the middle propeller downwash, the front propeller saw reduced loading near the 80% blade span in azimuth angles between 120 deg and 180 deg. The middle propeller showed similar features in azimuth angles between 180 deg and 240 deg due to the aft propeller downwash. The middle and aft propellers showed, correspondingly, increased loading around 80% span with a slight phase delay. Small tip-loading fluctuations on the front and middle propellers are also observed associated with specific rotor-rotor and rotor-wing interactions.

Figures 10(a) to 10(c) decompose the single-blade loading of configuration C1 to expose the interactions. In these plots, the loading signals had their mean values removed, and were then decomposed into primary and secondary parts through FFT. The primary part corresponds to the one-per-rev sinusoidal variation, which correlates well with the disk loading distributions of Figure 9. These were caused by the altered induction due to the compact arrangement of the rotors. For all configurations, the primary parts had a similar magnitude

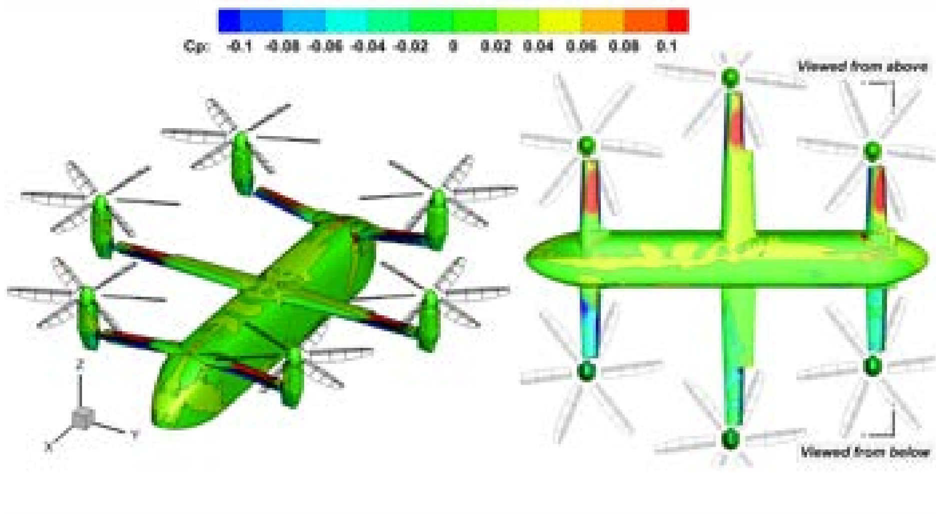

(a) C1.

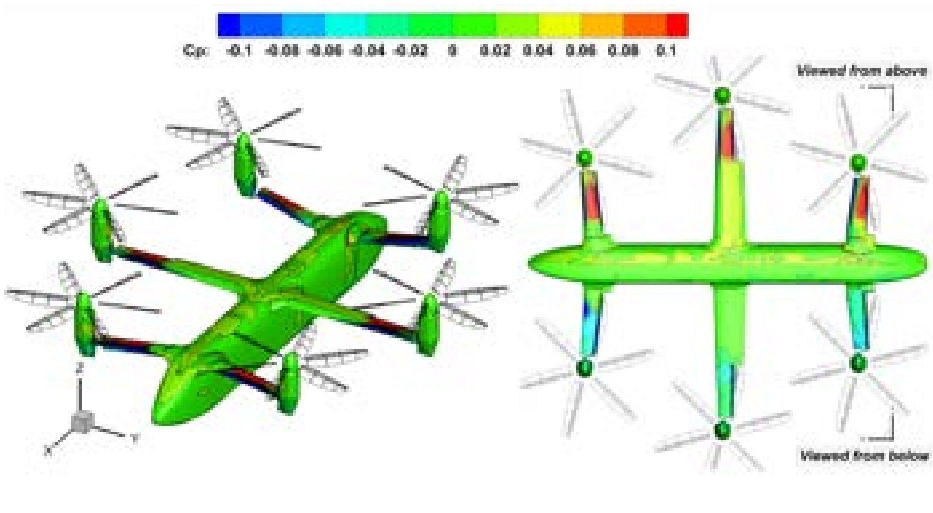

(b) C2.

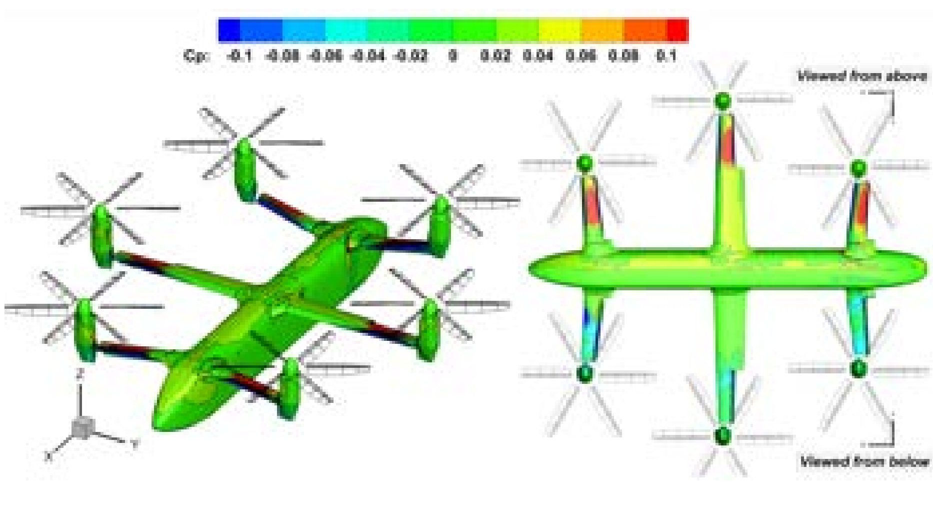

(c) C3.

Figure 7: Time-averaged surface C_p contours (normalised using blade tip speed) on the airframes.

Table 5: Airframe time-averaged downwash blockage forces ($\bar{F}_z$) and their standard deviations (std, $\sigma(F_z)$). All values are normalised using the MTOW.

Configurations	Front wings $\bar{F}_z$	Front wings $\sigma(F_z)$	Mid wings $\bar{F}_z$	Mid wings $\sigma(F_z)$	Aft wings $\bar{F}_z$	Aft wings $\sigma(F_z)$	Fuselage $\bar{F}_z$	Fuselage $\sigma(F_z)$
C1	-0.023	9.23E-04	-0.024	3.62E-04	-0.016	2.86E-04	-0.061	2.49E-03
C2	-0.023	1.13E-03	-0.024	2.85E-04	-0.017	3.13E-04	-0.030	3.01E-03
C3	-0.021	9.38E-04	-0.022	4.44E-04	-0.016	2.80E-04	-0.021	1.90E-03

Table 6: Time-averaged single rotor thrust ($\bar{T}$), and their standard deviations (std, $\sigma(T)$). All values are normalised by the MTOW.

Configurations	Front rotor $\bar{T}$	Front rotor $\sigma(T)$	Mid rotor $\bar{T}$	Mid rotor $\sigma(T)$	Aft rotor $\bar{T}$	Aft rotor $\sigma(T)$
C1	0.191	1.43E-03	0.193	7.49E-04	0.191	7.83E-04
C2	0.191	1.78E-03	0.194	1.11E-03	0.191	8.83E-04
C3	0.188	1.55E-03	0.190	1.55E-03	0.187	9.19E-04

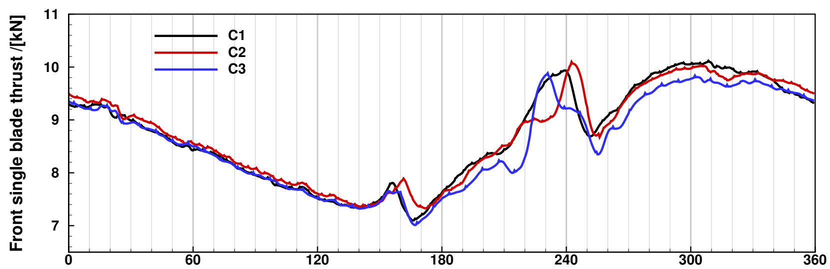

(a) Front propeller.

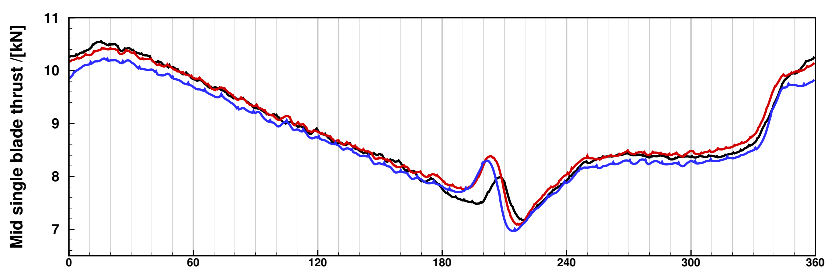

(b) Middle propeller.

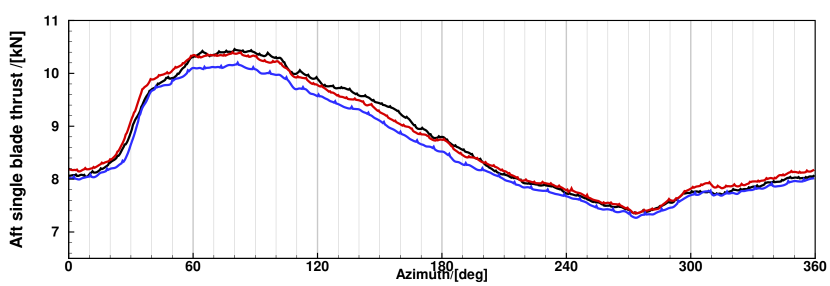

(c) Aft propeller.

Figure 8: Single propeller thrust loading variations for all configurations C1, C2, and C3.

of $\pm 1.2kN$ for a single blade.

The secondary components of the loading variations expose local interactions more clearly. Figure 10(d) presents the blade positions during the interactions. For the front blade in Figure 10(a), the secondary part showed two major deviations from the harmonic signals, one at $\Psi = 160$ deg (A) and the other around $\Psi = 240$ deg (B). Interaction A was caused by interactions with

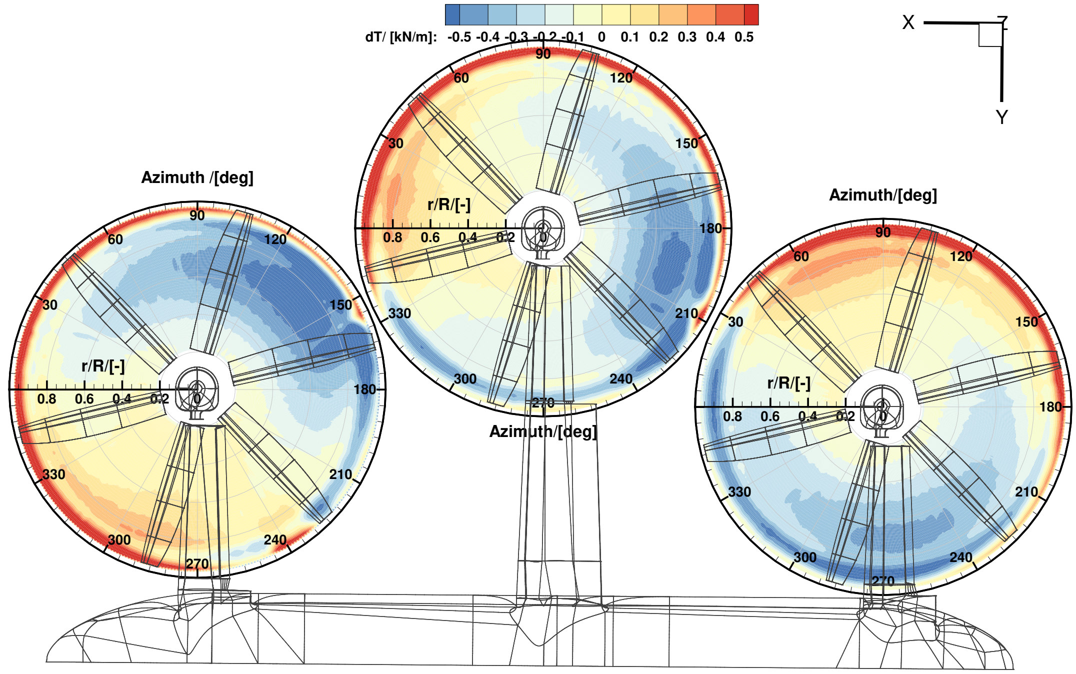

Figure 9: Disk loading variations due to aerodynamic interactions (relative to isolated rotors) for configuration C1.

the middle propeller during the blade encounter as shown in Figure 10(d). Since the middle blade was above the front blade, the front blade mostly experienced a reduction in the thrust and then gradually recovered as the blades move apart. Interaction B was due to interactions with the front wing and airframe. During this interaction, the front blade experienced a sudden jump in thrust, since it was upstream of the airframe and wing. For the front wing, the rotor-wing interaction (B) was the major disturbance.

For the middle blade in Figure 10(b), three points of interest can be noted. The first interaction C is from $\Psi = 330$ deg to 30 deg, which was caused by the blade encounter with the front propeller as shown in Figure 10(d). The second interaction D is at about $\Psi = 200$ deg, corresponding to interactions with the aft propeller through blade encounter. This is closely followed by interaction E point near $\Psi = 240$ deg. This was due to interactions with the middle wing and airframe. The third peak is near $\Psi = 360$ deg to 15 deg. For the middle propeller, all three interactions were of a similar magnitude and were closely followed.

For the aft blade in Figure 10(c), only one obvious peak can be noted. The interaction F was around $\Psi = 30°$, corresponding to the blade encounter with the middle propeller as shown in Figure 10(d). This was the major disturbance for the aft blade. A second fluctuation could be noted near $\Psi = 300°$ due to rotor-wing interactions, but this was only minor because of the aft propeller's clearance from the airframe.

5 Acoustics Analysis

5.1 Near-field Acoustics

This section discusses the near-field acoustic features of the Skybus vehicle in hover. The near-field acoustic data was directly extracted from the high-fidelity CFD. Due to the subsonic nature of the hover flow field, the far-field acoustic characteristics were dominated by the thickness (monopole) and loading (dipole) terms, especially the loading noise due to surface pressure variations. The near-field acoustic analysis of the Skybus vehicle hence begins with identifying the surface noise sources.

The root-mean-square (RMS) values of the surface sound pressure fluctuations of configurations C1, C2, and C3 are presented in Figures 11(a) to 11(c). Higher RMS values indicate stronger pressure fluctuations and consequently higher noise radiation. For C1 in Figure 11(a), the strongest variations concentrated near the wing/-fuselage junctions of the front and aft wings. The front wing junction, and much of the front wing upper surface showed particularly high RMS values, due to the strong rotor interactions which were discussed in the previous section. For the aft wing, high fluctuations were present on the fuselage below the wing, which should be associated with the rotor wake and its interactions with other surfaces. The middle wing saw strong fluctuations on sections below the rotor and near the wing/flap transition.

For C2 in Figure 11(b), a major difference compared to C1 was the reduction of pressure fluctuations on most

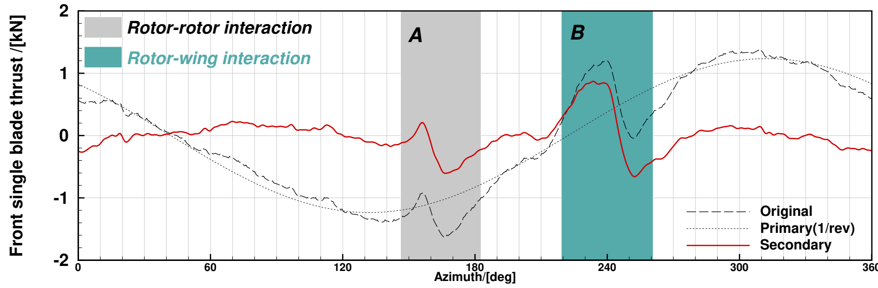

(a) Front propeller.

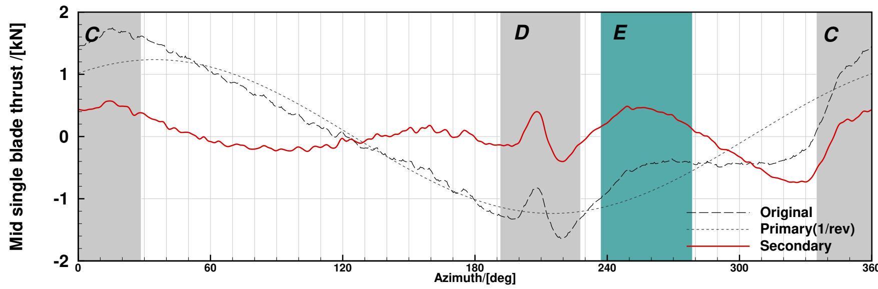

(b) Middle propeller.

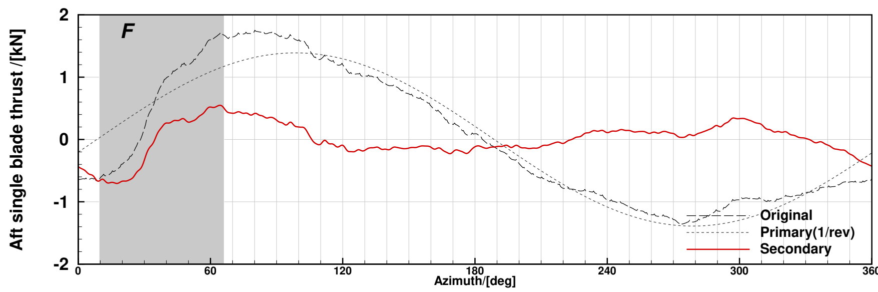

(c) Aft propeller.

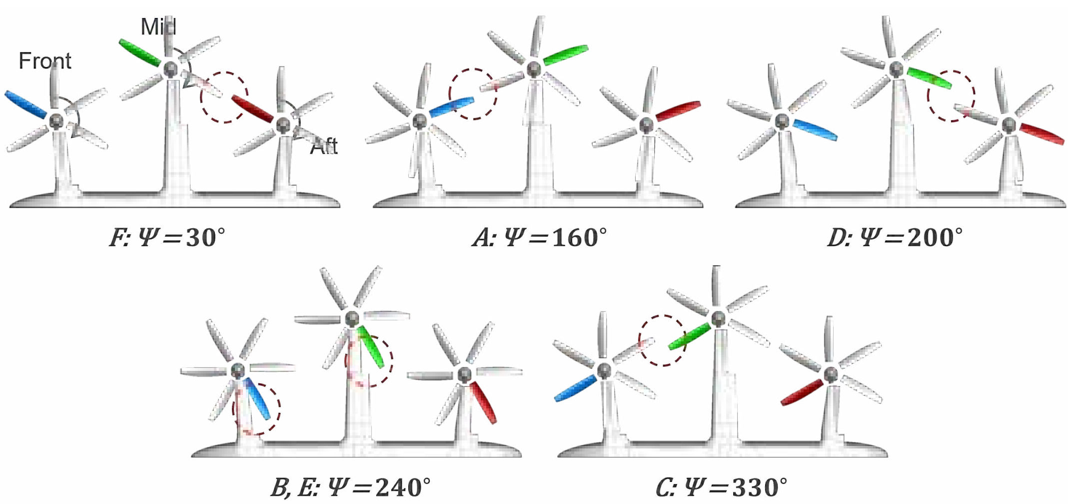

(d) Blade positions and interactions.

Figure 10: Decomposition of single propeller thrust loading variation for configuration C1.

of the fuselage surface. From C1 to C2, the fuselage fluctuation level was reduced from about 10 Pa RMS to about 5 Pa RMS. Apart from this, the surface acoustic characteristics remained similar to C1 despite differences in the airframe geometry. Strong pressure fluctuations were also present at the front and aft wing surfaces, their

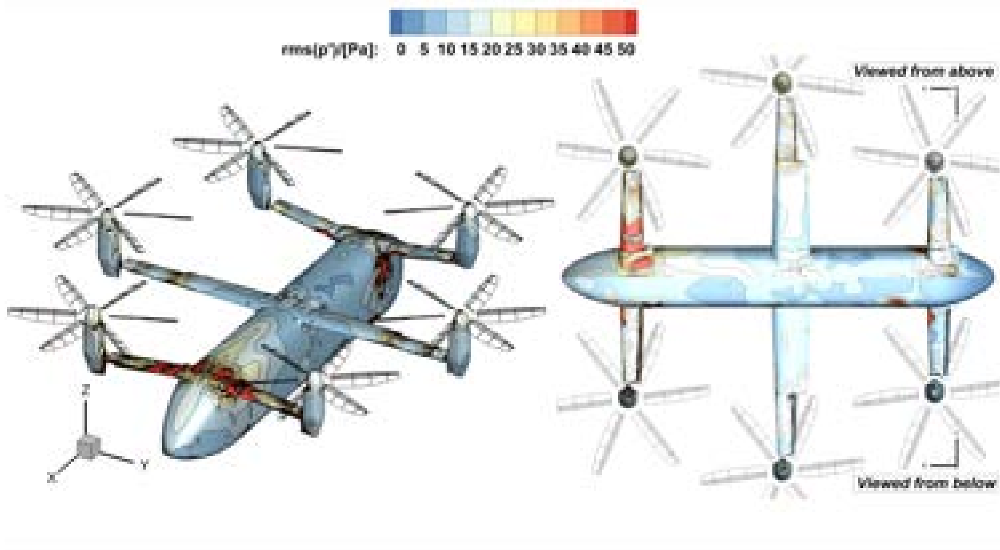

(a) C1.

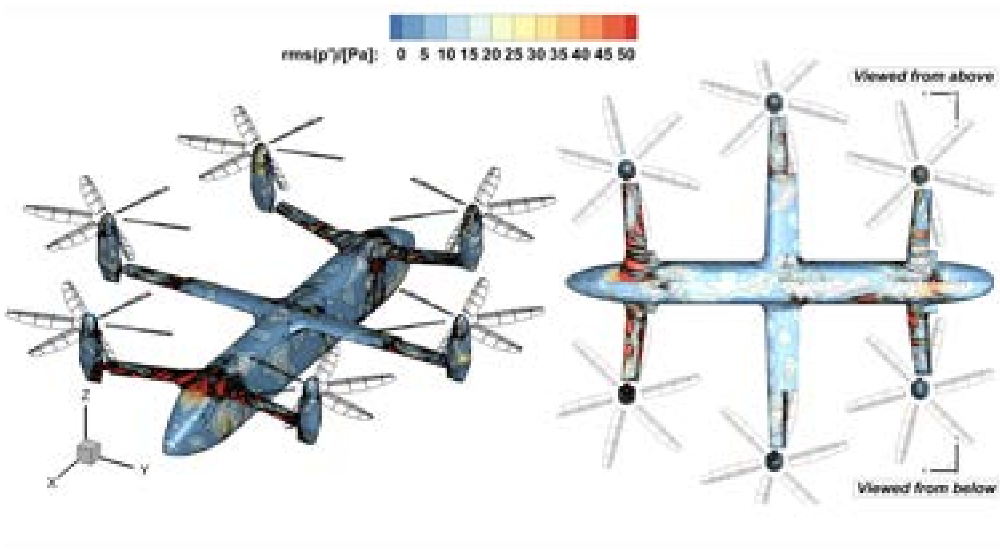

(b) C2.

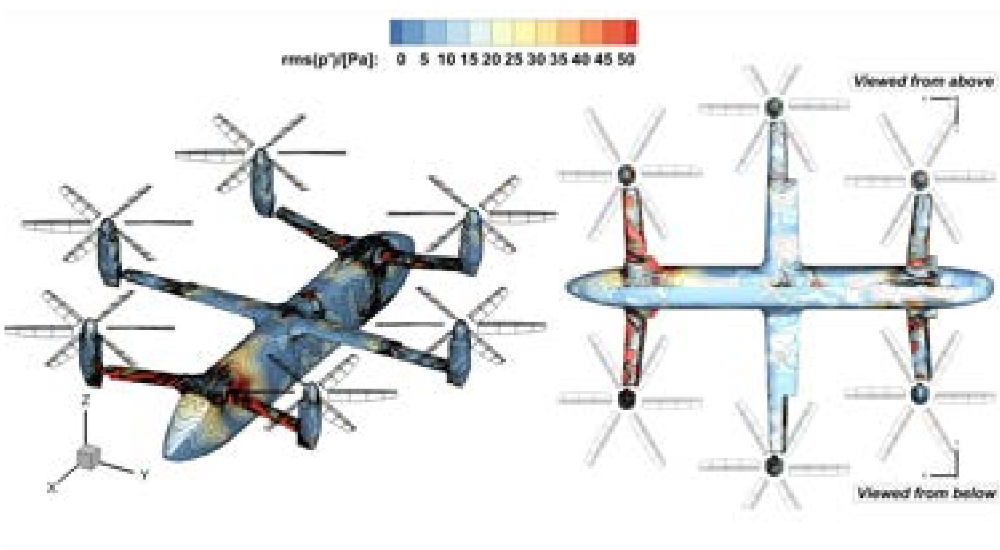

(c) C3.

Figure 11: Root-mean-square (RMS) contours of airframe surface sound pressure.

junctions with the fuselage, and at the flap sections of the middle wing.

For configuration C3 in Figure 11(c) with a different rotor design, there are some notable differences in the RMS distributions, but the magnitudes remain similar to C2. The major difference was at the front wing/-fuselage conjunction. C3 shows strong pressure fluctuations on the fuselage surface near the trailing edge of the wing, as opposed to the upper surface of C2 in Figure 11(b). This change also led to higher pressure RMS values on the front half of the fuselage surface. For the front wing, the pressure fluctuations were slightly decreased, while the aft wing fluctuations remained similar. These changes should be associated with the different acoustic directivity features of the revised blade design.

In addition to the surface acoustic sources, the present work also investigated near-field acoustic propagation, directivity, and frequency compositions. Figures 12(a) and 12(b) present the acoustic pressure field on a plane 3 metres below the C1 configuration, directly extracted from the high-fidelity HMB3 simulation on the fine grid of Table 3.

Figure 12(a) shows the instantaneous acoustic pressure field on the plane, overlapped by the vehicle outlines. The regions beneath the airframe and rotors were dominated by low-frequency and high-magnitude pressure fluctuations. These regions were dominated by rotor vortices, downwash, and airframe wake. Another high-fluctuations region was observed ahead of the vehicle along the x axis. This was associated with the clockwise (viewed from above) rotation of the port-side blades and pressure pulses due to the symmetry. Out of these regions, the acoustic field was dominated by high-frequency and low-magnitude pressure fluctuations carrying the acoustic waves to the far-field.

Figure 12(b) converts the acoustic signals to sound pressure levels (SPL). The high-SPL regions were noted beneath the rotors and the airframe, as well as a small region ahead of the cockpit along the x axis. These correlated well with the acoustic signals in Figure 12(a). Out of these regions, the SPL rapidly decreased. The SPL was reduced to about 90 dB at 20 metres away along the port-side direction. The near-field acoustic propagation showed a slight directivity towards the positive x axis, which corresponds to the vehicle cockpit and ahead of the aircraft.

For more quantitative discussions of the near-field acoustic propagation, acoustic signals perceived along an array of microphones below the middle wing and rotor (green dashed line in Figure 12(a)) was extracted and analysed. This microphone array overlaps with the middle wing and rotor and captures acoustic features due to the wing blockage and the rotor downwash.

The time-domain and frequency-domain compositions of the acoustic signals along the lateral array are shown in Figures 13(a) and 13(b), respectively. Figure 13(a) clearly shows three types of acoustic signals over two rotor revolutions. From the fuselage to the wing flap position, the acoustic signal was blended with various high- and low-frequency contents and was of medium strength. For regions below the rotor, the signal showed clear and strong low-frequency contents with a frequency of about one per revolution. In the free air region beyond the rotor boundary, the signal was characterised by high-frequency components of mild strength with a frequency of about six per revolution.

Figure 13(b) presents the frequency compositions of the acoustic signals along the lateral direction. The spectral magnitudes were normalised by their local maxima at each later position to highlight the frequency compositions. The frequency values were normalised by the blade passing frequency (BPF) to highlight the correlations. For regions near the fuselage and below the rotor, the dominant frequency had rich low-frequency components near 1/6 BPF, i.e. one per rotor revolution. For the near-fuselage regions, the signal also had weak high-frequency components corresponding to the BPF and its harmonics. For the free air region beyond the rotor boundary, the signal was dominated by the BPF and its harmonics.

The SPL variations along the microphone array are converted in Figure 14. Along the lateral direction, the acoustic magnitude fluctuated but gradually increased from 115 dB to the peak value of about 131 dB. The peak SPL value was at the outer board region of the rotor, and was due to the rotor wake. The obvious decrease before the peak should be associated with aerodynamic/acoustic shielding of the wing and flap. Moving away further along the later direction, the acoustic magnitude rapidly dropped to about 105 dB near the rotor boundary, then decreased following a mild and almost linear slope of about -1.5 dB/m. These differences indicate that the acoustics were dominated by different flow phenomena in the inner- and outer-board regions in the near-field.

For the Skybus design in hover, these analyses of the near-field acoustic propagation suggest that the rotor/airframe wake and downwash could dominate the near-field acoustics in regions downstream of the airframe and rotor. However, for regions free of the rotor and airframe wake flow, the acoustics was dominated by tonal components strongly correlating with the rotor blade passing.

5.2 Far-field Acoustics

This section discusses the far-field acoustics of the Skybus vehicle in hover. Far-field noise is critical for noise certification, as well as flight path programming and infrastructure design to minimise noise pollution. The far-field acoustics was computed using the HFWH2 code, taking the high-fidelity CFD results as input. The HFWH2 code solves the FW-H equations following Farassat's Formulation 1A [38]. The non-porous formulation was used in the current work due to the subsonic nature of the flow. This section will discuss the far-field acoustic levels and directivity, as well as perceived annoyance with tonal corrections.

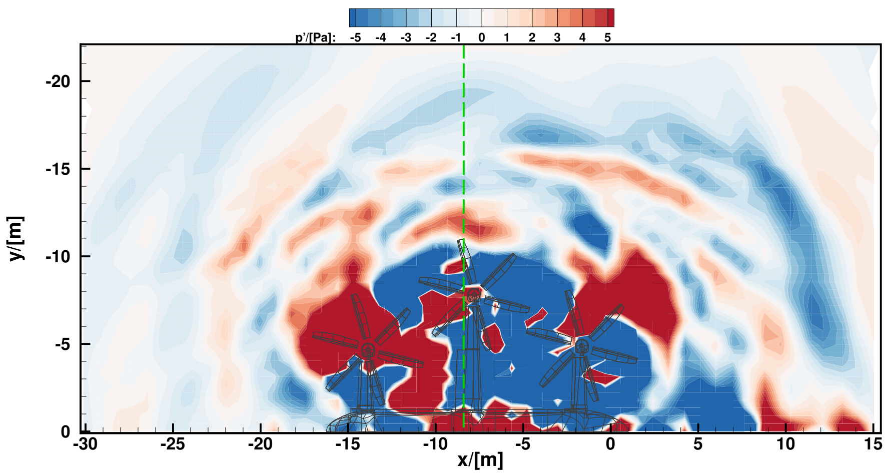

(a) Instantaneous acoustic signals.

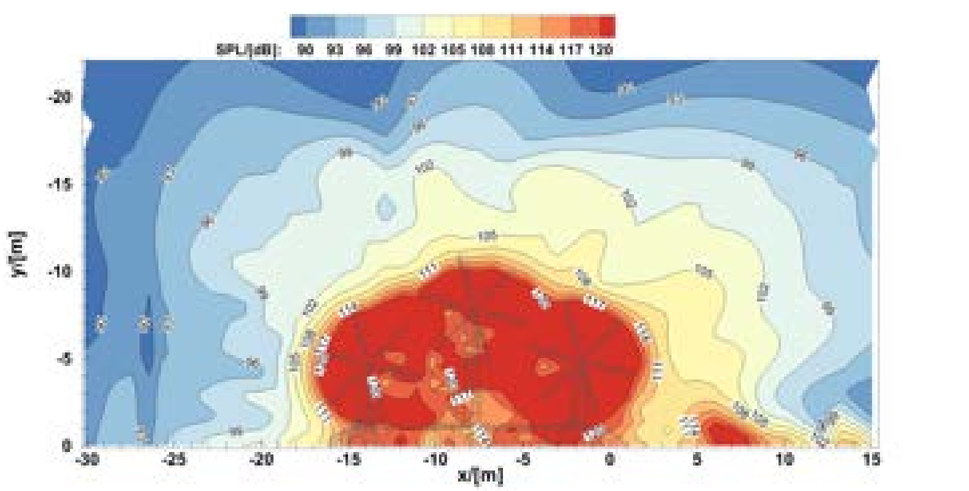

(b) SPL contours.

Figure 12: Acoustic signals and magnitudes on a plane 3 m below the C1 configuration.

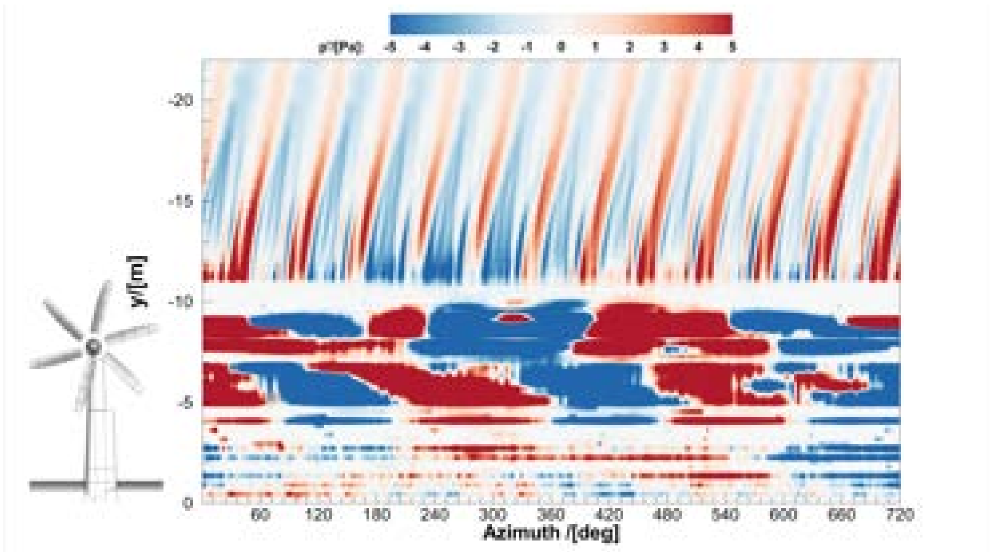

(a) Time-domain compositions.

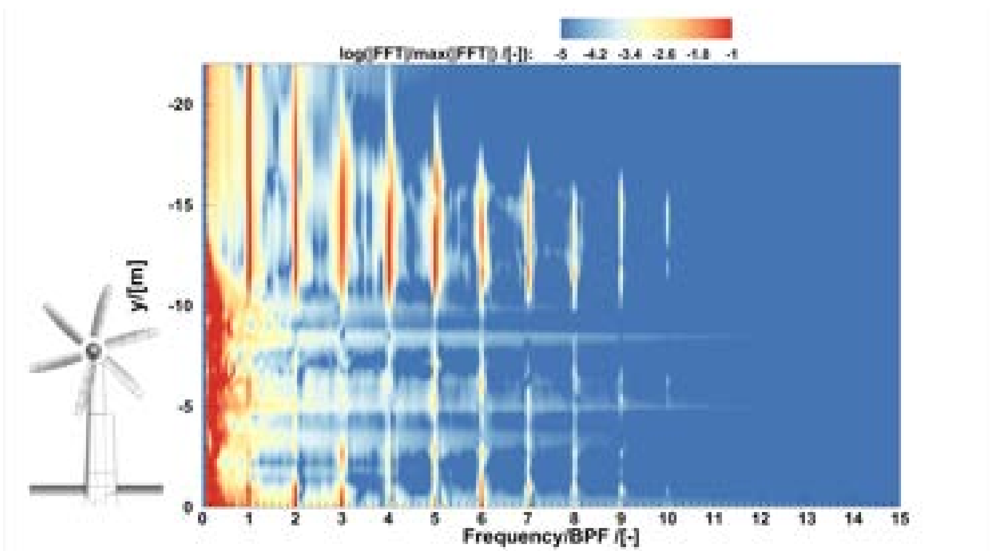

(b) Frequency-domain compositions.

Figure 13: Time-domain (a) and frequency-domain (b) compositions of acoustic signals perceived at the lateral microphone array (green dashed line of Figure 12(a)).

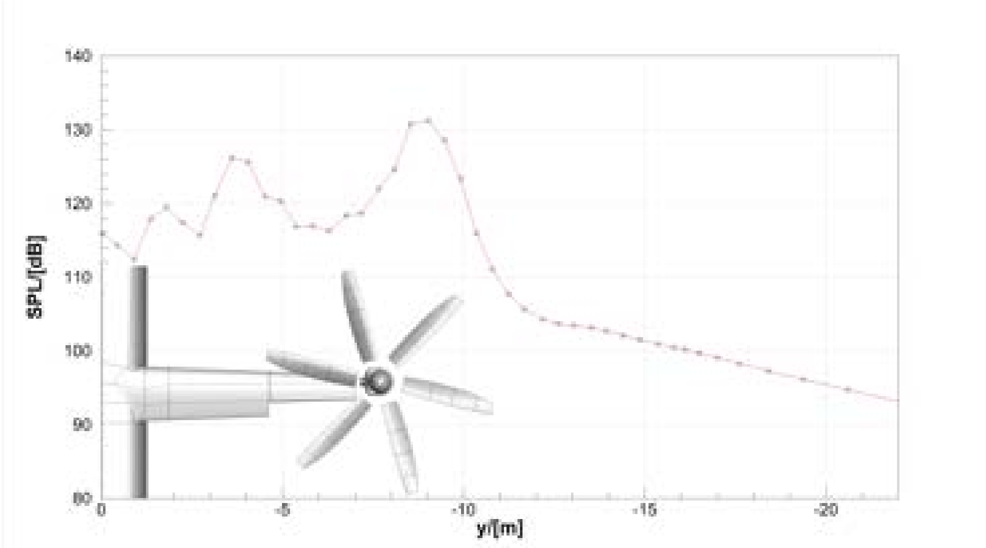

Figure 14: Sound pressure levels (SPL) variations along an array of microphones below the middle wing and rotor on a plane 3m below the C1 configuration(green dashed line in Figure 12(a)).

The far-field acoustics was computed at horizontal planes 50-m and 100-m below the vehicle, since ground noise is the primary concern in hover conditions. Figures 15(a) to 15(c) present the sound pressure level contours on a plane 50 metres below the vehicle. The vehicle position is denoted by wireframes. All three configurations showed similar acoustic directivity, despite differences in the magnitudes and the decay rate. For configuration C1 of Figure 15(a), the far-field acoustic radiation shows concentric patterns with the centre slightly ahead of the cockpit. These features correlated well with the near-field investigations in Figure 12(b). The maximum SPL was about 95 dB within a 50-metre radius around the vehicle. The acoustic strength decayed quickly at a rate of about -0.1 dB/m as the distance from the vehicle increased. Beyond 150 metres in the lateral direction, the noise was lower than 78 dB, but the decay slowed to about -0.05 dB/m.

Figure 15(b) presents the far-field acoustic features for configuration C2 with the revised airframe designs. Compared to C1, the acoustic characteristics remained similar, except that the magnitudes were slightly lower. The peak acoustics was also about 95 dB, but high-noise areas were confined in smaller regions along the lateral and longitudinal directions. This should be associated with the reduced aerodynamic interactions on the fuselage according to aerodynamic analyses in the previous section. The noise decay slowed down at about 100 metres away. Hence the noise distributions further away from the vehicle shared more similarities with C1.

Figure 15(c) presents the SPL contours for configuration C3. Despite the concentric patterns, the acoustic distributions of C3 differ considerably from C1 and C2. The maximum noise was still of about 95 dB, and the high-noise region was larger than C2 but smaller than C1. However, the noise decay was much slower than C1 and C2, especially in the lateral direction. At 100 metres away, the SPL is still about 86 dB. At 250 metres away, the SPL was about 80 dB, as opposed to the 74 dB for C1 and C2. These differences were brought by the revised blade design. Despite the improved aerodynamic performance, these blades considerably altered acoustic characteristics through their different directivity features and interactions with other components.

Figures 16(a) to 16(c) present the SPL contours on a horizontal plane 100 metres below the vehicle in hover. For all configurations, the acoustic strength decreased due to the increased vertical distance from the vehicle. The maximum SPL was about 90 dB within a small region below the vehicle for all configurations. The propagation features remained similar to Figures 15(a) to 15(c), but became more irregular due to the increased distance allowing more mixture of the noise. Configuration C3 in Figure 16(c) still shows slower noise decay to the far field.

This section also presents acoustic results perceived in noise certification scenarios. It should be highlighted that, up to now, there is still no established noise certification for rotorcraft in hover flight. The hover condition is most similar to the approach flight scenario of the existing noise certification, as illustrated in Figure 17. In this analysis, the Skybus vehicle stays 120 m above the ground, and we will focus on acoustic signals perceived at (0, -150, -120) m on the starboard side for all three configurations.

For configurations C1, C2, and C3, the noise signals perceived at (0, -150, -120) m were decomposed into spectral components and converted into SPL, as well as A-weighted SPL values. These are presented in Figures 18(a) to 18(c). The frequency values were normalised using the BPF. This highlighted that the dominant frequencies of the acoustic signals were the BPF and its harmonics for all three configurations.

The SPL plots showed the most acoustic energy con-

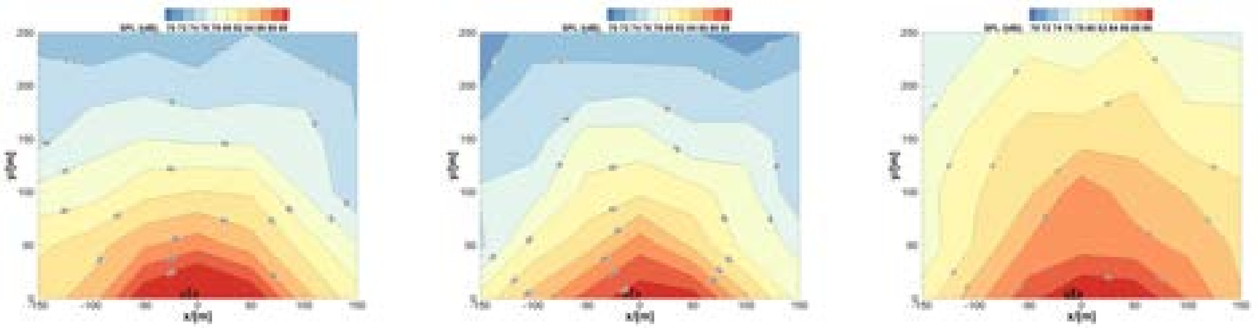

(a) C1.

(b) C2.

(c) C3.

Figure 15: Far-field acoustic SPL contours at 50 m below the vehicle in hover.

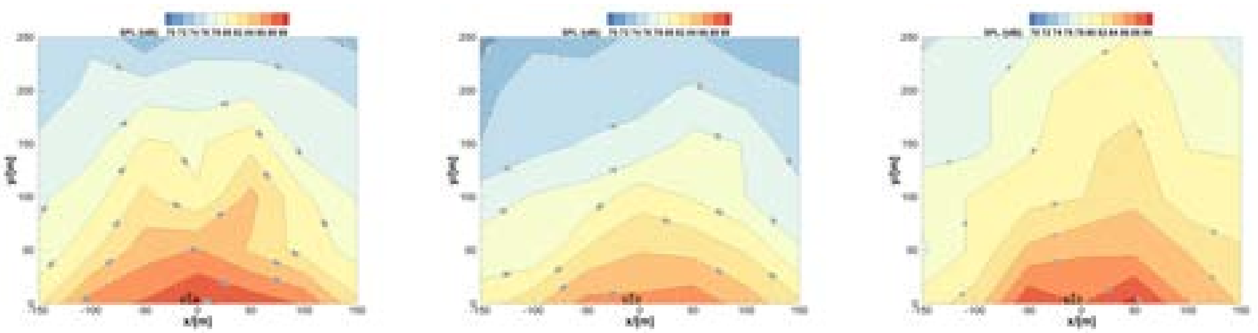

(a) C1.

(b) C2.

(c) C3.

Figure 16: Far-field acoustic SPL contours at 100 m below the vehicle in hover.

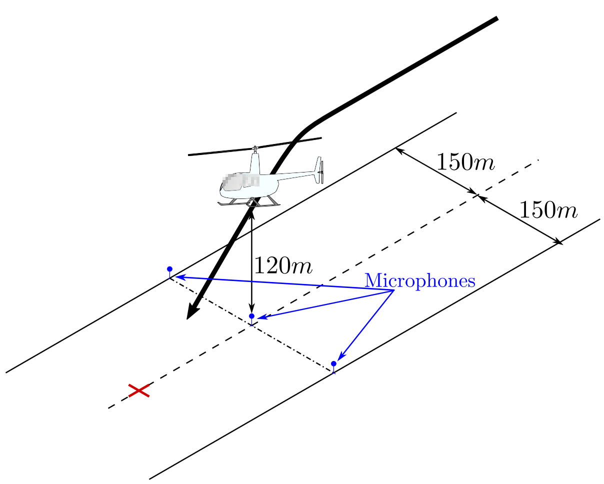

Figure 17: Noise certification for helicopter approach.

centrated in low-frequency components within the first 10 to 15 BPFs. From C1 in Figure 18(a) to C2 in Figure 18(b), the low-frequency components showed mild reductions in strength by about 2 dB. There were notable reductions of 5 to 10 dB in strength for high-frequency components beyond the 40th BPF. This was associated with the reduced fuselage interactions leading to lower high-frequency noise radiation. For C3 in Figure 18(c), while the low-frequency components remained similar to C2, the high-frequency components stabilised around 45 dB. This correlated well with its stronger near-field surface pressure variations and stronger far-field noise radiation discussed in previous sections.

With tonal corrections emphasising frequencies more sensitive to human hearing, the A-weighted SPL plots show that the stronger low-frequency components were lowered for all configurations. This highlights the acoustic benefit of the low RPM design of the Skybus vehicle. The highest A-weighted SPL was about 60 dB near the 10th BPF. The strength of higher-frequency components was very slightly increased by the A-weighting, but the change was negligible.

To correlate better with the noise certification, as well as to further highlight the annoyance per human perception, the Effective Perceived Noise Level (EPNL) was computed from the raw noise signals perceived at (0, -150, -120) m. The EPNL metric reflects the noise annoyance level over a period of exposure time and is widely used for aircraft noise certification. The EPNL computation in this work followed the classic 10-step procedure [45, 46].

Note that the EPNL computation requires integration over a short time window near the maximum PNLT (Perceived Noise Level with Tonal corrections) values. However, in the present hover case, the PNLT stays constant since the source-receiver distance never changes. The duration time hence had to be assumed for the EPNL computation in this work.

Figure 19 shows the EPNL variations subject to different hover durations for all three configurations. The EPNL value increased quickly from 0 to 60-s duration, but became asymptotic for longer durations. Configuration C1 showed the highest EPNL values. Configuration C2 showed the lowest EPNL level, about 2-3 EPNdB lower than C1, with the revised airframe design. The EPNL of C3 was in between C1 and C2. This again indicates that the revised blade design balanced the acoustic performance with the aerodynamic improvement.

The dashed line in Figure 19 represents the certificate EPNL limit of 101.24 EPNdB for an equivalent helicopter of the same weight when approaching. For the Skybus design, all configurations were well below this limit for short hover durations. For C1, the maximum duration time is 8 minutes. C3 improves this to 10 minutes, while C2 improves this to 12 minutes.

6 Conclusions

This work presented high-fidelity aerodynamic and acoustic analyses of the heavy-lift Skybus design in hover flight. Three configurations with different airframe and blade designs were modelled using the HMB3 CFD framework with scale-adaptive turbulence modelling. The aerodynamic performance, interactions, and impacts of the design changes were discussed in detail. The near- and far-field acoustic features of the vehicle were also computed and analysed. The following conclusions can be drawn from the current study:

1. For the baseline Skybus design (C1), the airframe led to a blockage force of 0.13 of the MTOW of 14,000 kg. The overall power consumption was about 4200 kW in hover. Despite their different positions, the overall thrust and power were almost evenly distributed among the front, middle, and aft propellers. By increasing the distance between the propellers along the longitudinal direction and shrinking the fuselage width, configuration C2 reduced the airframe downwash to 0.1 MTOW. The rotor thrust and power changes were negligible. Configuration C3 with the revised blade design reduced the overall power by 3% compared to the baseline, and the airframe downwash was further reduced by 0.01 MTOW.

2. For the Skybus configuration, the fuselage is an important source of the blockage, rather than the wings with flaps below the propellers. In the baseline configuration C1 with the wide fuselage, the fuselage blockage accounted for 50% of the overall blockage. Reducing the fuselage width in C2 reduced this percentage to 25%. Slightly reducing the rotor thrust in C3 reduced the overall blockage on the wings and the fuselage. In all configurations, the front and middle wings contributed about 0.023 MTOW of the overall blockage, while the aft wing suffered a lighter downwash of 0.017 MTOW thanks to its clearance from the aft propeller. All airframe components showed small absolute loading variations in time, suggesting that the mean rotor downwash is the primary impact on the airframe in hover.

3. For all configurations, the rotor blades experienced similar sinusoidal variations due to interactions altering the wake downwash and contraction. The blade loading distributions showed increased tip loading in outer regions clear of the interactions, and decreased tip loading in inner regions towards the airframe. This phenomenon correlated well with previous studies on rotors in compact configurations[12]. Apart from the primary sinusoidal variation, the rotor blades also had small loading fluctuations corresponding to specific local interactions, i.e. blade encounter and rotor/wing interactions. However, the absolute loading varia-

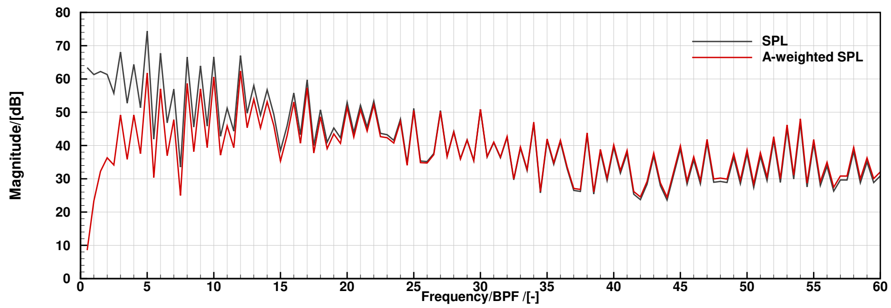

(a) C1.

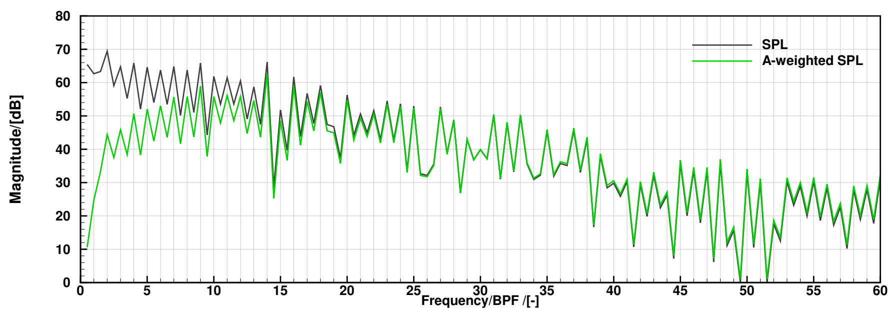

(b) C2.

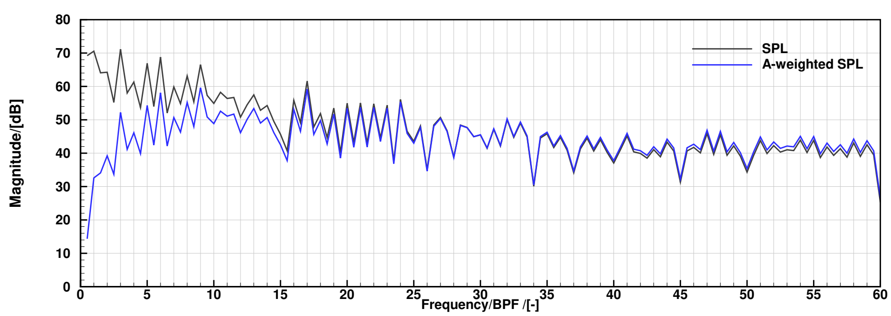

(c) C3.

Figure 18: Frequency compositions and A-weighted tonal corrections of acoustic signals perceived at the approach certification point (0, -150, -120)m for all configurations C1, C2, and C3.

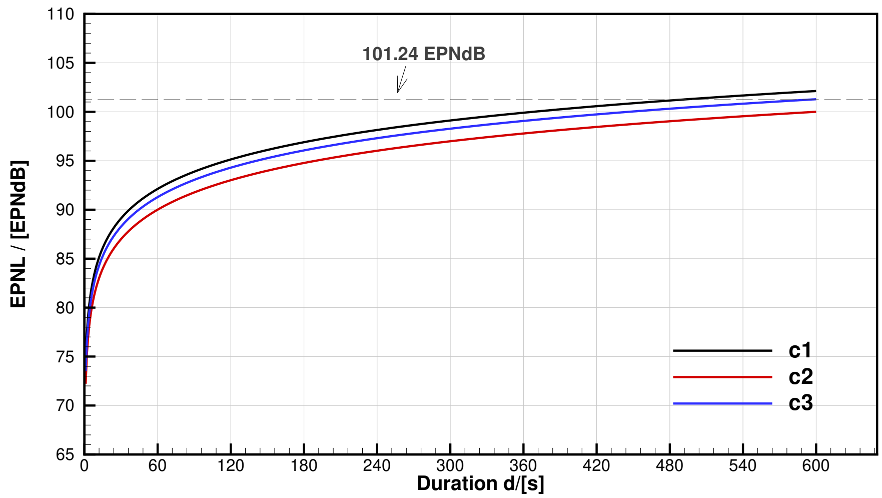

Figure 19: EPNL perceived at the approach certification point (0, -150, -120)m for all configurations C1, C2, and C3, and the variation with hover duration.

tions were minor compared to the mean propeller thrust. Design modifications had minor impacts on the phase and magnitudes of these local interactions.

4. In the near-field and below the hovering Skybus vehicle, the acoustics features were dominated by the strong airframe and rotor wake systems. In this region, the acoustics had a range of frequencies below the BPF and mostly near the 1/6 BPF. Beyond the rotor outer boundary in the lateral direction and in the free air, the acoustics was characterised by high-frequency and low-amplitude propagation. The dominant frequencies were the BPF and its harmonics. The acoustic magnitudes peaked under the propeller wake but quickly decayed in the surrounding area.

5. The design modifications has strong acoustic impact despite their lesser aerodynamic impact. By reducing the fuselage width and increasing the rotor clearance, configuration C2 effectively reduced the acoustic fluctuations on the fuselage. Although aerodynamically more efficient, the revised blades in configuration C3 resulted in more acoustic fluctuations on the fuselage. These near-field features were consistent with their respective far-field noise characteristics. In the far field 50- and 100-m below the vehicle in hover, the maximum acoustic strengths were about 95 dB and 90 dB in SPL, respectively. The BPF and its harmonics dominated the spectral components. All three configurations showed similar noise directivity in the longitudinal direction, especially ahead of the cockpit. Configuration C2 showed shrunk high-noise regions below the vehicle compared to C1. C3 also had small high-noise regions, but the noise decay was much slower than C1 and C2 due to differences in the blades. This highlights the necessity of integrated and multi-disciplinary design and optimisation for eVTOL vehicles.

6. Despite the heavy weight of the Skybus eVTOL, the perceived noise level in the certification scenarios was acceptable. This was partially due to the low rotor RPM that scaled down the strongest noise strength at low frequencies of human perception. The EPNL of all configurations with short hover durations was well below the certification limit of 101.24 EPNdB of an equivalent helicopter approaching. The longest possible hover duration for configurations C1, C2, and C3 before reaching the annoyance limit was about 8 minutes, 12 minutes, and 10 minutes, respectively.

Future work on the Skybus design will continue and focus on vehicle trimming and integrated design optimisation.

Acknowledgement

The authors would like to acknowledge GKN Aerospace for their support and kind permission to publish this work. The authors also would like to acknowledge the Sulis Tier 2 HPC platform hosted by the Scientific Computing Research Technology Platform, funded by EPSRC Grant EP/T022108/1 and the HPC Midlands+ consortium. Part of the results were obtained using the ARCHIE-WeSt High Performance Computer (www.archie-west.ac.uk).

Bibliography

[1] Filippone, A. and Barakos, G., "Rotorcraft systems for urban air mobility: A reality check," *The Aero-*

nautical Journal, 2020, pp. 1–19.

[2] Öhrle, C., Schaferlein, U., Keßler, M., and Krämer, E., "Higher-order Simulations of a Compound Helicopter using Adaptive Mesh Refinement," *the AHS International 74th Annual Forum & Technology Display, Phoenix, Arizona, USA*, 2018.

[3] Öhrle, C., Frey, F., Thiemeier, J., Kebler, M., and Krämer, E., "Coupled and Trimmed Aerodynamic and Aeroacoustic Simulations for Airbus Helicopters' Compound Helicopter RACER," *Journal of the American Helicopter Society*, Vol. 64, 07 2019, pp. 1–14.

[4] Frey, F., Thiemeier, J., Öhrle, C., Keßler, M., and Krämer, E., "Aerodynamic Interactions on Airbus Helicopters' Compound Helicopter RACER in Cruise Flight," *Journal of the American Helicopter Society*, Vol. 65, No. 4, 2020, pp. 1–14.

[5] Frey, F., Öhrle, C., Thiemeier, J., Keßler, M., and Krämer, E., "Aerodynamic Interactions on Airbus Helicopters' Compound Helicopter RACER in Hover," *Vertical Flight Society 76th Annual Forum*, 10 2020.

[6] Thiemeier, J., Öhrle, C., Frey, F., Keßler, M., and Krämer, E., "Aerodynamics and flight mechanics analysis of Airbus Helicopters' compound helicopter RACER in hover under crosswind conditions," *CEAS Aeronautical Journal*, Vol. 11, No. 1, 2020, pp. 49–66.

[7] Ventura Diaz, P., Johnson, W., Ahmad, J., and Yoon, S., "Computational study of the side-by-side urban air taxi concept," *Vertical Flight Society's (VFS) Annual Forum and Technology Display*, No. ARC-E-DAA-TN67955, 2019.

[8] Ventura Diaz, P. and Yoon, S., "Computational study of NASA'S quadrotor urban air taxi concept," *AIAA SciTech 2020 Forum*, 2020, p. 0302.

[9] Sagaga, J. and Lee, S., "Acoustic Predictions for the Side-by-Side Air Taxi Rotor in Hover," *Proceedings of the 77th VFS Forum, Online*, 2021, pp. 10–14.

[10] Miesner, S., Keßler, M., and Kramer, E., "Investigation of Near Ground Effects in Hover Flight for the Multi-Rotor Aircraft Volocopter 2X," *The Vertical Flight Society's 76th Annual Forum And Technology Display, Virtual*, 2020.

[11] Miesner, S., Keßler, M., Kramer, E., and Schaferlein, U., "High-fidelity Simulation of the Volocopter-2X in Cruise Flight," *The Vertical Flight Society's 77th Annual Forum And Technology Display, Virtual, May 10–14*, 2021.

[12] Miesner, S., Keßler, M., Kramer, E., and Schaferlein, U., "High-fidelity Simulations of Rotors in Compact Configuration," *The Vertical Flight Society's 78th Annual Forum And Technology Display, USA, May 10–12*, 2022.

[13] Boisard, R., Lefevre, L., Zhang, T., Barakos, G., Visingardi, A., Lößle, F., Kostek, A., Andronikos, T., Keßler, M., Wickersheim, R., Colli, A., Gibertini, G., and Zanotti, A., "Rotor/Rotor aerodynamic interactions–A Garteur Action Group," *33rd Conference of the International Council of the Aerospace Sciences (ICAS22), Stockholm, Sweden, 4-6 September*, 2022.

[14] Zhang, T. and Barakos, G. N., "High-fidelity numerical investigations of rotor-propeller aerodynamic interactions," *Aerospace Science and Technology*, Vol. 124, 2022, pp. 107517.

[15] Healy, R., Gandhi, F., and Mistry, M., "Computational Investigation of Multirotor Interactional Aerodynamics with Hub Lateral and Longitudinal Canting," *AIAA Journal*, Vol. 60, No. 2, 2022, pp. 872–882.

[16] Sugawara, H. and Tanabe, Y., "Numerical Investigation of Rotor/Wing Aerodynamic Interactions at High Advance Ratios," *Journal of Aircraft*, Vol. 56, No. 6, 2019, pp. 2285–2298.

[17] Lim, J. and Tran, S., "Interactional structural loads of the xv-15 rotor in airplane mode," *Proceedings of the 45th European Rotorcraft Forum, Warsaw, Poland*, 2019, pp. 17–20.

[18] Lim, J., "Fundamental Investigation of Proprotor and Wing Interactions in Tiltrotor Aircraft," *The VFS 75th Annual Forum & Technology Display, Philadelphia, Pennsylvania, the USA*, 02 2021.

[19] Higgins, R. J., Zarev, A., Barakos, G. N., and Green, R. B., "Numerical investigation of a two-bladed propeller inflow at yaw," *Journal of Aircraft*, Vol. 57, No. 2, 2020, pp. 292–304.

[20] Russell, C. and Conley, S., "The multirotor test bed–a new NASA test capability for advanced VTOL rotorcraft configurations," *VFS Forum*, Vol. 76, 2020.

[21] Zhang, T., Barakos, G. N., Foster, M., et al., "Multi-fidelity aerodynamic design and analysis of propellers for a heavy-lift eVTOL," *Aerospace Science and Technology*, Vol. 135, 2023, pp. 108185.

[22] Zhang, T., Barakos, G. N., Foster, M., et al., "High-fidelity aerodynamic and acoustic design and analysis of a heavy-lift eVTOL," *Aerospace Science and Technology*, Vol. 137, 2023, pp. 108307.

[23] Steijl, R., Barakos, G. N., and Badcock, K., "A framework for CFD analysis of helicopter rotors in hover and forward flight," *International Journal for Numerical Methods in Fluids*, Vol. 51, No. 8, 2006, pp. 819–847.

[24] Babu, S. V., Zografakis, G., Barakos, G. N., and Kusyumov, A., "Evaluation of scale-adaptive simulation for transonic cavity flows," *International Journal of Engineering Systems Modelling and Simulation*, Vol. 8, No. 2, 2016, pp. 106–124.

[25] Biava, M., Woodgate, M., and Barakos, G. N., "Fully implicit discrete-adjoint methods for rotorcraft applications," *AIAA Journal*, Vol. 54, No. 2, 2015, pp. 735–749.

[26] Antoniadis, A., Drikakis, D., Zhong, B., Barakos, G., Steijl, R., Biava, M., Vigevano, L., Brocklehurst, A., Boelens, O., Dietz, M., et al., "Assessment of CFD methods against experimental flow measurements for helicopter flows," *Aerospace Science and Technology*, Vol. 19, No. 1, 2012, pp. 86–100.

[27] Steijl, R. and Barakos, G., "CFD analysis of complete helicopter configurations–lessons learnt from the GOAHEAD project," *Aerospace Science and Technology*, Vol. 19, No. 1, 2012, pp. 58–71.

[28] Garcia, A. J. and Barakos, G. N., "Numerical simulations on the ERICA tiltrotor," *Aerospace Science and Technology*, Vol. 64, 2017, pp. 171–191.

[29] Zhang, T. and Barakos, G. N., "Toward Vehicle-Level Optimization of Compound Rotorcraft Aerodynamics," *AIAA Journal*, Vol. 60, No. 3, 2022, pp. 1937–1957.

[30] Jarkowski, M., Woodgate, M., Barakos, G., and Rokicki, J., "Towards consistent hybrid overset mesh methods for rotorcraft CFD," *International Journal for Numerical Methods in Fluids*, Vol. 74, No. 8, 2014, pp. 543–576.

[31] Menter, F. and Egorov, Y., "A scale adaptive simulation model using two-equation models," *43rd AIAA aerospace sciences meeting and exhibit*, 2005, p. 1095.

[32] Menter, F. and Egorov, Y., "The scale-adaptive simulation method for unsteady turbulent flow predictions. Part 1: theory and model description," *Flow, Turbulence and Combustion*, Vol. 85, No. 1, 2010, pp. 113–138.

[33] Rotta, J., "über eine methode zur berechnung turbulenter scherströmungsfelder," *Zeitschrift Angewandte Mathematik und Mechanik*, Vol. 50, No. 1-4, 1970, pp. 204–205.

[34] Chirico, G., Barakos, G. N., and Bown, N., "Propeller installation effects on turboprop aircraft acoustics," *Journal of Sound and Vibration*, Vol. 424, 2018, pp. 238 – 262.

[35] Zhang, T. and Barakos, G. N., "High-fidelity numerical analysis and optimisation of ducted propeller aerodynamics and acoustics," *Aerospace Science and Technology*, Vol. 113, 2021, pp. 106708.

[36] Higgins, R., Barakos, G., Shahpar, S., and Tristanto, I., "A computational fluid dynamic acoustic investigation of a tiltwing eVTOL concept aircraft," *Aerospace Science and Technology*, Vol. 111, 02 2021, pp. 106571.

[37] Ffowcs Williams, J. E. and Hawkings, D. L., "Sound generation by turbulence and surfaces in arbitrary motion," *Philosophical Transactions of the Royal Society of London. Series A, Mathematical and Physical Sciences*, Vol. 264, No. 1151, 1969, pp. 321–342.

[38] Farassat, F., "Derivation of Formulations 1 and 1A of Farassat," Tech. rep., NASA / TM-2007-214853, 2007.

[39] Dighe, V. V., Avallone, F., and van Bussel, G., "Effects of yawed inflow on the aerodynamic and aeroacoustic performance of ducted wind turbines," *Journal of Wind Engineering and Industrial Aerodynamics*, Vol. 201, 2020, pp. 104174.

[40] Smith, D. A., Filippone, A., and Barakos, G. N., "Acoustic Analysis of Counter-Rotating Open Rotors with a Locked Blade Row," *AIAA Journal*, 2020(avialable online).

[41] Zhang, T., Qiao, G., Smith, D., Barakos, G., and Kusyumov, A., "Parametric study of aerodynamic performance of equivalent ducted/un-ducted rotors," *Aerospace Science and Technology*, Vol. 117, 2021, pp. 106984.

[42] Zhang, T. and Barakos, G. N., "High-Fidelity CFD Validation and Assessment of Ducted Propellers for Aircraft Propulsion," *Journal of the American Helicopter Society*, Vol. 66, No. 1, 2021, pp. 1–28.

[43] Jimenez-Garcia, A. and Barakos, G., "Assessment of a high-order MUSCL method for rotor flows," *International Journal for Numerical Methods in Fluids*, Vol. 87, No. 6, 2018, pp. 292–327.

[44] Roache, P. J., "Perspective: A Method for Uniform Reporting of Grid Refinement Studies," *Journal of Fluids Engineering*, Vol. 116, No. 3, 09 1994, pp. 405–413.

[45] Edge Jr, P. M. and Cawthorn, J. M., "Selected methods for quantification of community exposure to aircraft noise," Tech. rep., 1976.

[46] May, D. and Watson, E., "Correction Procedures for Aircraft Noise Data. Volume IV. Tone Perception." Tech. rep., WYLE LABS EL SEGUNDO CALIF, 1980.